

Microstructural heterogeneity and mechanical anisotropy of 18Ni-330 maraging steel fabricated by selective laser melting: The effect of build orientation and height

Yi Yao¹, Kaiwen Wang², Xiaoqing Wang^{3,4,a)}, Lin Li^{1,b)}, Wenjun Cai^{2,c)}, Samuel Kelly^{3,4}, Natalia Esparragoza^{3,4}, Matthew Rosser^{3,4}, Feng Yan¹

¹Department of Metallurgical and Materials Engineering, The University of Alabama, Tuscaloosa, AL 35401, USA

²Department of Materials Science and Engineering, Virginia Polytechnic Institute and State University, Blacksburg, VA 24061, USA

³Department of Applied Engineering, Jacksonville State University, Jacksonville, AL 36265, USA

⁴The Center for Manufacturing Support, Jacksonville State University, Jacksonville, AL 36265, USA

^{a)}Address all correspondence to these authors. e-mail: xwang@jsu.edu

^{b)}e-mail: lin.li@eng.ua.edu

^{c)}e-mail: caiw@vt.edu

Received: 5 February 2020; accepted: 5 May 2020

Distinguished by a marked combination of high strength and high fracture toughness, 18Ni-300 maraging steel (MS) is widely used for intricate tool and die applications. MS is also amenable to the powder bed fusion additive manufacturing process, providing unique opportunities to make small features and incorporate cooling channels in molds. In this study, tensile test samples were fabricated using selective laser melting to investigate the effects of built height and orientations on the evolution of the microstructure and the mechanical properties of the samples. The microstructure of the as-fabricated samples consists of the primary α -martensite phase and fine cellular microstructure (~ 0.66 – 0.83 μm) with the retained austenite γ -phase aggregated at the boundaries of the cells, resulting in an enhanced mechanical performance compared with traditional counterparts under the same condition (without post-heat treatments). Random grain orientations with weak textures are revealed in all samples. The XY-built samples display better tensile performance when compared to the Z-built samples due to the fine grain sizes and the retained γ phase. The bottom of the Z-built sample exhibits a higher hardness than other parts of the sample, which could be attributed to its finer cellular structure.

Introduction

Powder bed fusion (PBF) is one of the most mature and widely used additive manufacturing (AM) process, during which the powdered material is selectively consolidated by melting using a heat source such as laser [1] or electron beam [2]. As one of the typical PBF-AM process, the laser PBF-AM process, also named as selective laser melting (SLM) or direct metal laser sintering (DMLS), can produce functional metal components with nearly full density, high-dimensional precision, good surface integrity [3], and outstanding mechanical properties [4, 5]. SLM is applicable to various metals, such as Inconel alloys [6] and steels [7], and it has a strong appeal to the industry targeting low-volume production for specific applications [8] as it can provide unique opportunities to manufacture tools with complex shapes, containing inner channels for conformal cooling [9].

Maraging steel (MS) is the material of choice for many tooling applications, including plastic injection molding, high-pressure die casting, punching, and extrusion, due to its high specific strength and fracture toughness [10]. The notably high strength of MS is attributed to its microstructure which is typically characterized by a martensitic matrix with a high number density of nanometer-sized precipitates of different types of intermetallic phases, such as Ni_3Mo , Ni_3Ti , Ni_3Al , and Fe_2Mo [11]. As a special class of low-carbon steel, the low-carbon level (below 0.03%) in MS leads to its excellent welding and toughness characteristics [12], which makes it suitable for the SLM processing [11].

The standard 300 grade MS, also called 18Ni-300 MS or 1.2709 (X3NiCoMoTi 18-9-5) MS, is the most commercially applicable material for the SLM process. The SLM technology is an efficient method to expand application circumstances and

fields of MS [13], such as conformal cooling injection tooling [14, 15], which could reduce the cycle time by up to 70% for blow molding and 20% for die casting. To achieve such high-performance molds and dies, it is important to understand the microstructure and properties of SLM-fabricated maraging steels [16]. However, due to the complexity of the SLM process, many processing factors, such as raw powder, manufacturing process parameters, and post-heat treatments, influence the microstructure and properties of the produced parts, requiring systematic investigation [17].

Studies have been conducted in recent years to produce SLM solid parts of MS with mechanical performance comparable to those by the conventional routes. Mutua et al. [18] investigated the influences of various process parameters on the density, surface morphology, microstructure, and mechanical properties of 18Ni-300 MS fabricated by a LUMEX Avance-25 system. They were able to produce reliable products with relatively high density and good surface quality. In the study of Conde et al. [19], the as-built MS samples were characterized by a very fine cellular-dendritic structure with a trace amount of austenite phase, about 4%, because of the inhomogeneous distribution of alloying elements [20]. With heat treatments, the samples show higher strengths in the *X*- and *Y*-directions as compared to the *Z*-direction, similar to those reported by Monkova et al. [21]. Mooney et al. [22] studied the effect of built orientations and heat treatments on the plastic anisotropy of 18Ni-300 MS produced by one EOS M280 system, identifying that the as-built samples present a significant plastic anisotropy [23] which can be reduced by aging heat treatment. In addition, heat treatment condition was optimized for the as-built 18Ni-300 MS, under which strength and wear resistance can be maximized [24, 25]. The optimum heat treatment is determined by various conditions, such as the initial condition of the microstructure induced by the raw powder and processing parameters [26]. So far, limited studies have been conducted on the microstructural heterogeneity and mechanical anisotropy of the as-fabricated parts along the build direction or in various planes of the samples. Comprehensive studies are still needed to understand the manufacturing process and achieve finishing parts with desired properties for various industrial applications.

In this work, the vertical and horizontal built 18Ni-300 MS parts were manufactured using an EOS M290 machine to investigate the evolution of the microstructure and the mechanical properties. The microstructure of the 18Ni-300 MS was characterized and analyzed via optical microscopy (OM), X-ray diffraction (XRD), and scanning electron microscopy (SEM), and electron backscatter diffraction (EBSD). The mechanical properties were measured by tensile and microhardness tests. The effects of the built orientation and built height on the microstructure and mechanical properties were elucidated.

Results and Discussion

A. Microstructure analysis

The typical optical microstructure in the *X*-plane and the *Z*-plane of the as-built SLM 18Ni-300 MS sample with different built orientations are shown in Fig. 1. Different built orientations lead to different configurations of the melt pool. The longitudinal direction of the melt pool is perpendicular to the longitudinal plane of the *Z*-built sample, as illustrated in Figs. 1(a) and 1(b), but it is parallel to the longitudinal plan of the *XY*-built plane, as shown in Figs. 2(c) and 2(d). The morphology of the melt pool exhibits little difference between the two samples with different orientations and the different locations of the *Z*-built sample. The fish-scale melt pool profile and the laser beam scanning tracks were observed clearly in the *X*-plane of the *XY*-built and the *Z*-built samples. Additionally, the 67° rotation of the stripes hatch pattern between contiguous layers was revealed clearly in the *X*-plane of the *XY*-built and the *Z*-built samples. The melt tracks have a width of around 110 μm, which is about the hatch spacing size, and a depth of 40 μm corresponding to the layer thickness. This has been attributed to the Gaussian distribution of laser intensity [13] and the discontinuous nature of the laser scan-melting process [18]. Fine cellular dendrites with the growth direction along the built direction (*Z*-axis) were observed, which is caused by the extremely high cooling rate in the process [27].

In addition, porosity and other solidification defects induced are also revealed in Fig. 1, as marked by the white circles, which are mainly located at the boundaries of the melt pools or the keyhole of the melt pool. The spherical gas pores marked in the images can be traced back to the gas entrapped inside the powder particles during the powder atomization process [28, 29] or the vapor results from the unstable keyhole melting mode due to the high laser power density [30]. These defects are detrimental to the mechanical properties of the produced components [31, 32], which can be minimized by hot isostatic pressing [33, 34].

The microstructure of the as-fabricated SLM 18Ni-300 MS sample under SEM is shown in Fig. 2. Fine cellular microstructures were formed within the molten tracks due to the high cooling rate ($\sim 10^7$ °C/s [35]) during the rapid cooling process of the SLM process. It is a very typical microstructure in SLM-fabricated samples, also identified in SLM Inconel 718 [36]. As shown in Fig. 2, the cellular microstructures displayed various orientations along the built direction, which is determined by the temperature gradient (*G*) and growth rate (*R*) that vary within a melt pool [37]. As shown in Figs. 2(c), 2(e), and 2(g), along with the built height, more and more dendrites can grow from the former layer to the subsequent layer. This is attributed to the heterogeneous nucleation in the first few deposited layers due to the heat sink effect of the stainless

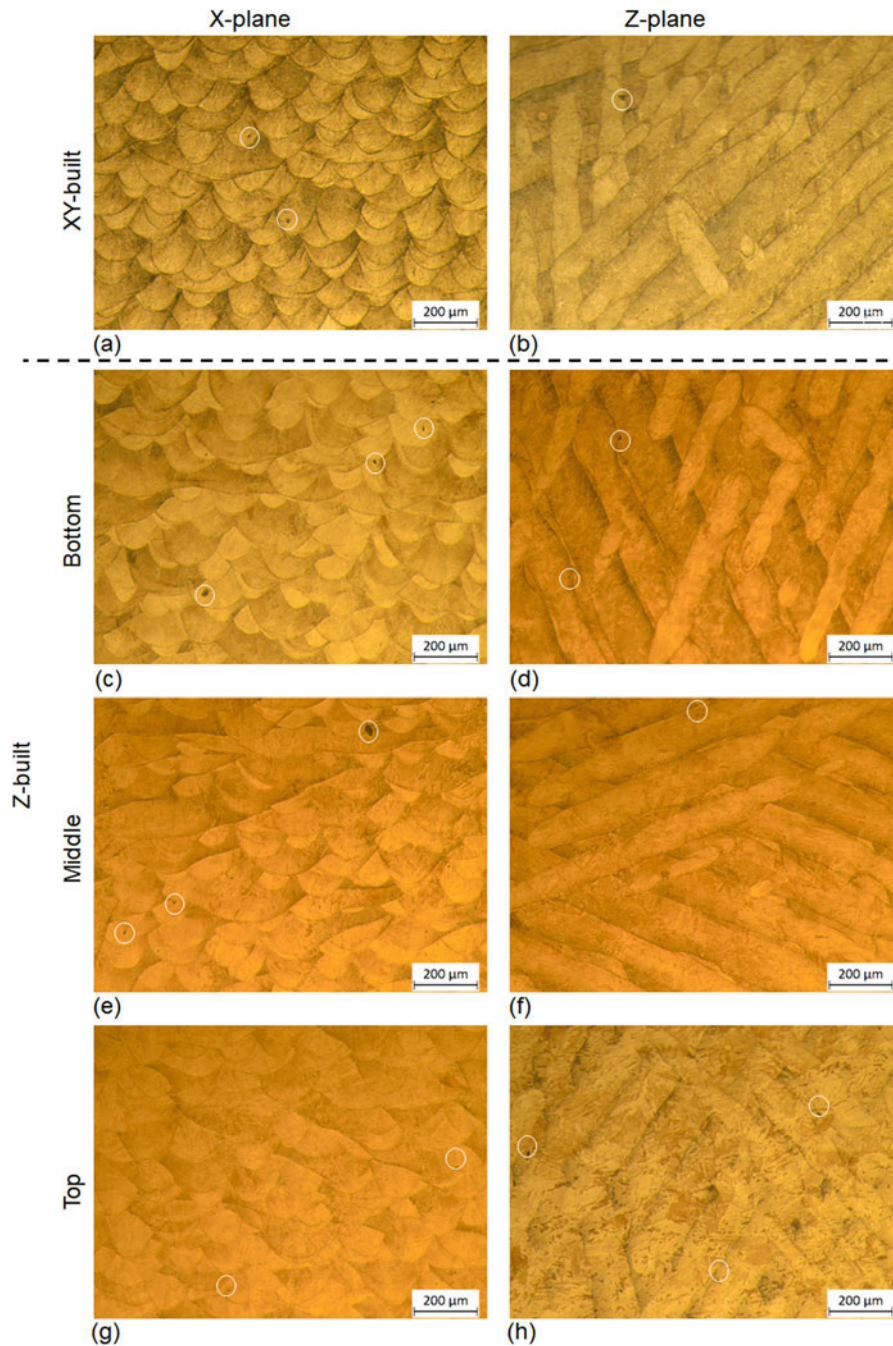


Figure 1. OM of the as-built SLM 18Ni-300 MS samples from the (a,b) XY-built, (c,d) Z-built—bottom, (e,f) Z-built—middle, and (g,h) Z-built—top. Note: white circle zones indicate the defects.

steel substrate plate. With the increase of the built height, the occurrence of the epitaxial nucleation becomes predominantly and the dendrites grow subsequently along the thermal gradient. This is mainly caused by the heat loss diffusing peripherally from epitaxial the melt pool in the plane to the former solidified parts as the laser beam scanning and re-melting the previously solidified layers. This also can be seen from the Z-plane of the sample, and the cellular dendrites at the bottom

location present tilted growth directions to the beam scanning plane [Fig. 2(d)] and gradually display nearly parallel growth directions to the build direction.

Fig. 3(a) provides an example of the calculation procedure of the average cellular size using the line intercept method, where the cellular size is measured vertical to the long axis of the cells. The calculated average cellular size of the different heights at the Z-built and the XY-built samples is summarized

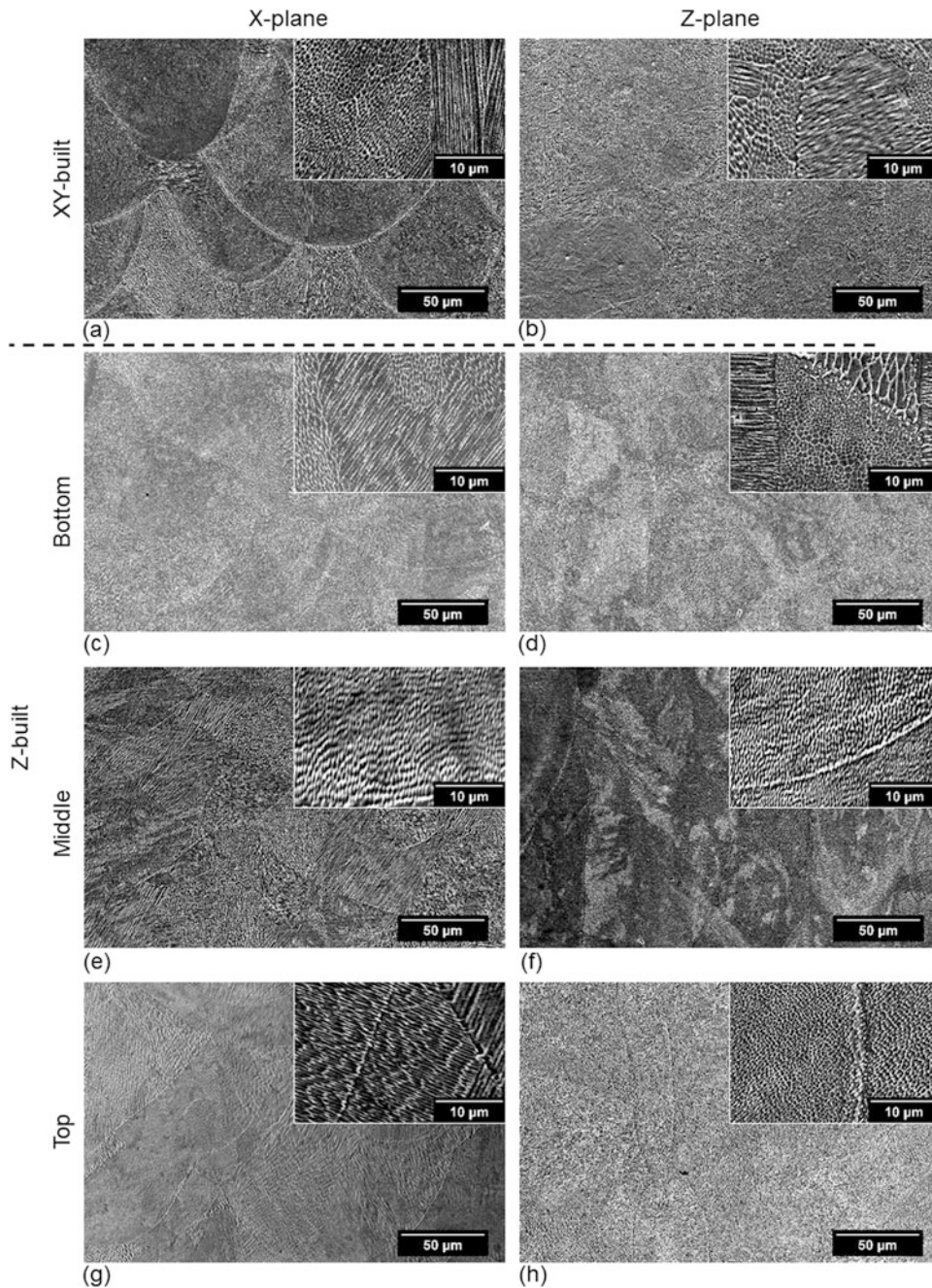


Figure 2. SEM of the as-built SLM 18Ni-300 MS samples from the (a,b) XY-built, (c,d) Z-built—bottom, (e,f) Z-built—middle, and (g,h) Z-built—top. Note: white circle zones indicate the defects.

in Fig. 3(c). This fine microstructure contributes to the enhanced hardness and strength of SLM steels when compared with conventionally manufactured steels, following the Hall–Petch relationship [38]. There is no significant difference in the size of the cellular microstructure, all falling in the range of 0.66–0.83 μm. Only the top location of the Z-built sample displays a higher value, which is caused by the lower cooling rate during solidification.

The SLM process primarily produces the α -martensite phase with the minor retained austenite γ phase in bright color aggregated at the fine cellular boundaries, as marked as P1 and P2 in Fig. 3(a). The Energy Dispersive Spectroscopy (EDS) analysis of the two areas found that the white area (P2) presents a higher content in Ni, Ti, Al, Mo, and Co than the dark area (P1), as listed in Fig. 3(b). It forms when the melt material cools rapidly from austenite finish to ambient

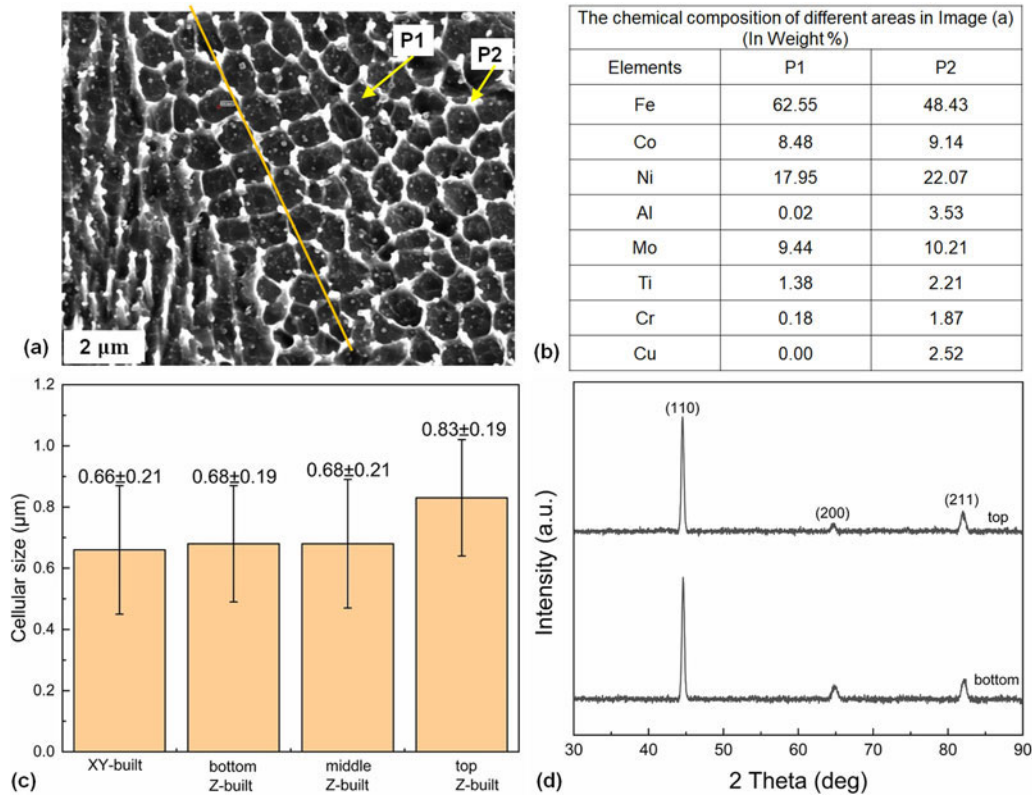


Figure 3. (a) The high magnification SEM for the calculation of the average cellular size and (b) the EDS analysis of the two areas P1 and P2 shown in (a). (c) The average cellular sizes of samples at the different height of the Z-built and the XY-built samples. (d) The XRD patterns of the Z-built samples at different built heights.

temperature, essentially freezing in place solute-rich austenite and leaving it untransformed [22] at the boundary. In addition, the XRD patterns from the bottom and top of the Z-built sample [shown in Fig. 3(d)] can only resolve the α -martensite matrix, indicating the low content of the austenite phase if any.

The typical grain morphologies in the Z-plane and the X-plane of the Z-built sample are shown in Fig. 4. The Z-plane exhibits extremely fine equiaxed (uniformly distributed at the center of a laser track) and columnar grains (perpendicularly distributed at the edge of the laser track), as illustrated in Fig. 4(a). The grain morphology in the SLM sample depends on the heat input (Q_s) distribution, temperature gradient (G), and growth rate (R). The morphology in the Z-plane could be related to the Q_s distribution caused by the Gaussian laser energy distribution, expressed as follows [39]:

$$Q_s = \frac{fP_v}{\pi d^2 h} \exp\left(-3\frac{R^2}{d^2}\right) \left(1 - \frac{h}{z}\right) \quad (1)$$

where f is the factor of heat distribution that influences the power distribution, P_v is the laser power absorptions in terms of surface, d is the beam radius, R is the radial distance from the beam center, h is the current depth in the thickness direction, and z is the depth of the energy source. The distribution of

Q_s at the Z-plane is also overlapped in Fig. 4(a). Notably, the Q_s decreases with the increase of R . The temperature at the center of the laser track is much higher than the temperature at the edge, leading to a higher supercooling degree at the center. Therefore, the molten metal at the center is expected to have a high nucleation rate, facilitating the formation of the equiaxed grains. On the other hand, the low temperature (due to the small heat input) at the edge suppresses the nucleation and the thermal flux from the center to edge causes the formation of columnar grains.

The typical microstructure of the X-plane is shown in Fig. 4 (b). The columnar and equiaxed grains distribute at the bottom and center of the molten pool, respectively. The morphology of grain at the X-plane is determined by the ratio of G and R [40]. As mentioned before, G at the bottom is higher than that at the center due to the heat distribution. For the same reason, R at the bottom is much lower than that at the center. So the larger G/R at the bottom leads to the columnar grains, and the smaller G/R at center results in the equiaxed grains [13].

Fig. 5 shows the EBSD inverse pole figure (IPF) maps obtained on the X-plane of the Z-built sample [Fig. 5(a)] and the Z-plane of the XY-built sample [Fig. 5(b)]. A clear columnar structure could be seen in Fig. 5(a) along the Z-axis, i.e., the growth direction, which has been revealed in most alloys

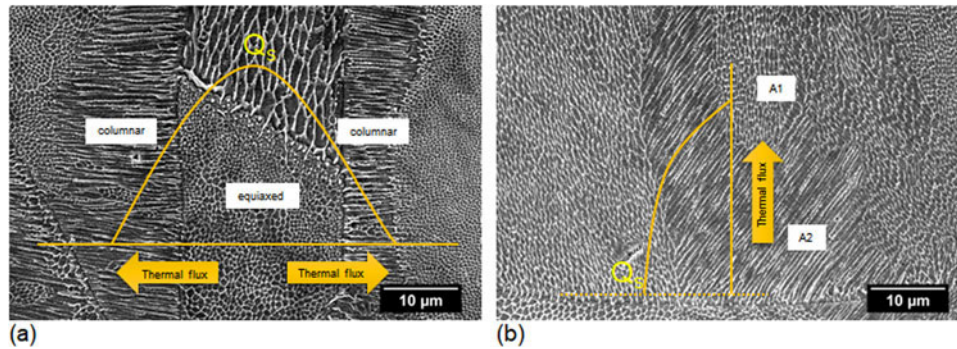


Figure 4. The typical microstructure of (a) the *X*-plane and (b) the *Z*-plane of the *Z*-built sample. In (b), Region A1 means smaller *G/R* → equiaxed grains and Region A2 means larger *G/R* → columnar grains.

fabricated by PBF-AM processes [35]. The growth direction is perpendicular to the laser tracks due to the temperature gradient and heat distribution, indicating that the epitaxial nucleation occurs and grows from the former layer to the straight after layer during the solidification process [41]. The orientation map of the *Z*-plane shows intersected scanning lines with 67°, matching with the scanning strategy with 67° between scanning directions of adjacent layers, as illustrated in Fig. 5(b). Moreover, both IPFs show random grain orientations, i.e., the absence of profound crystallographic texture. The pole figures (PFs), shown in Figs. 5(c) and 5(d), further confirm that the texture in the two samples is very weak. The non-textured structure could be related to the 67° rotation, which changes the heat flux direction [23, 42]. The grain size distribution is shown in Fig. 5(e). The *X*-plane of the *Z*-built sample shows a relatively larger grain size than that of the *Z*-plane of the *XY*-built sample, and the average grain size of the *X*-plane and the *Z*-plane is 14.36 and 6.68 μm, respectively.

B. Mechanical Properties

The tensile properties and microhardness of the SLM 18Ni-300 MS samples are summarized in Table I. The engineering strain–stress curves of two samples are shown in Fig. 6(a). The yielding strength (σ_y) and the tensile strength (σ_{UTS}) are both higher than those of the conventional counterparts without heat treatments [43], which could be attributed to the fine cellular microstructure as discussed in Sec. A. However, the as-built samples have much lower values when compared to conventional counterparts after heat treatment, which indicated the importance of heat treatments in improving the mechanical performance of the as-produced samples. The *XY*-built sample shows higher tensile performance than that of the *Z*-built sample, not only in the strength (~8%) but also in the ductility. This property anisotropy is caused by the columnar structure formed during the solidification process, as shown in Fig. 5(a). Compared to the literature counterparts, the as-built samples have comparable

tensile properties with the values in the literature, such as the tensile strength which are in the range of 1010–1325 MPa [16, 18, 19, 21–24, 43–51].

As shown in Table I, the samples have a comparable or larger hardness than the values in the literature [44, 45]. The sample built with orientation in the *XY*-plane (*XY*-built) presents a higher hardness than the sample vertical built in the *XZ*-plane (*Z*-built). This also has been reported in previous studies [22, 44, 52]. Moreover, the *XY*-built sample and the bottom of the *Z*-built sample show higher hardness values than those at the middle and top of the *Z*-built samples. The better mechanical performance in the bottom built parts is most likely due to the finer cellular or grain structure, as shown in Fig. 3(a). By comparing the microhardness values in the *X*-plane and the *Z*-plane, it is found that the slight anisotropy (4.06%) exists in different directions of the print samples, which results from the orientation differences of the cellular dendrites between the *X*-plane and the *Z*-plane.

In order to further analyze the deformation behavior, the true stress and strain hardening rate changing along with the true strain curves are plotted and calculated in Fig. 6(b). Obviously, the strain hardening rates of the two curves linearly drop after yielding, indicating the low strain hardening ability in the two SLM MS samples. Necking occurs at 1% and 2% strain for the *XY*-built and the *Z*-built samples, respectively, at which the strain hardening rate equals the true stress (i.e., Considere criterion). Indeed, the fractographic observation also verifies that the occurrence of necking. The low strain hardening ability may come from the fine grain size and the solidification defects. The heated MS always exhibits higher strength but lower ductility, which results from the precipitation strengthening that blocks the motion of dislocations [45], while in the as-fabricated MS, the absence of the hard and brittle precipitate leads to a better ductility but weaker strength. As shown in Fig. 6(b), the strain hardening rate of the *Z*-built sample is higher than that of the *XY*-built sample immediately after yielding but decreases more rapidly after necking and falls below zero. This accounts for

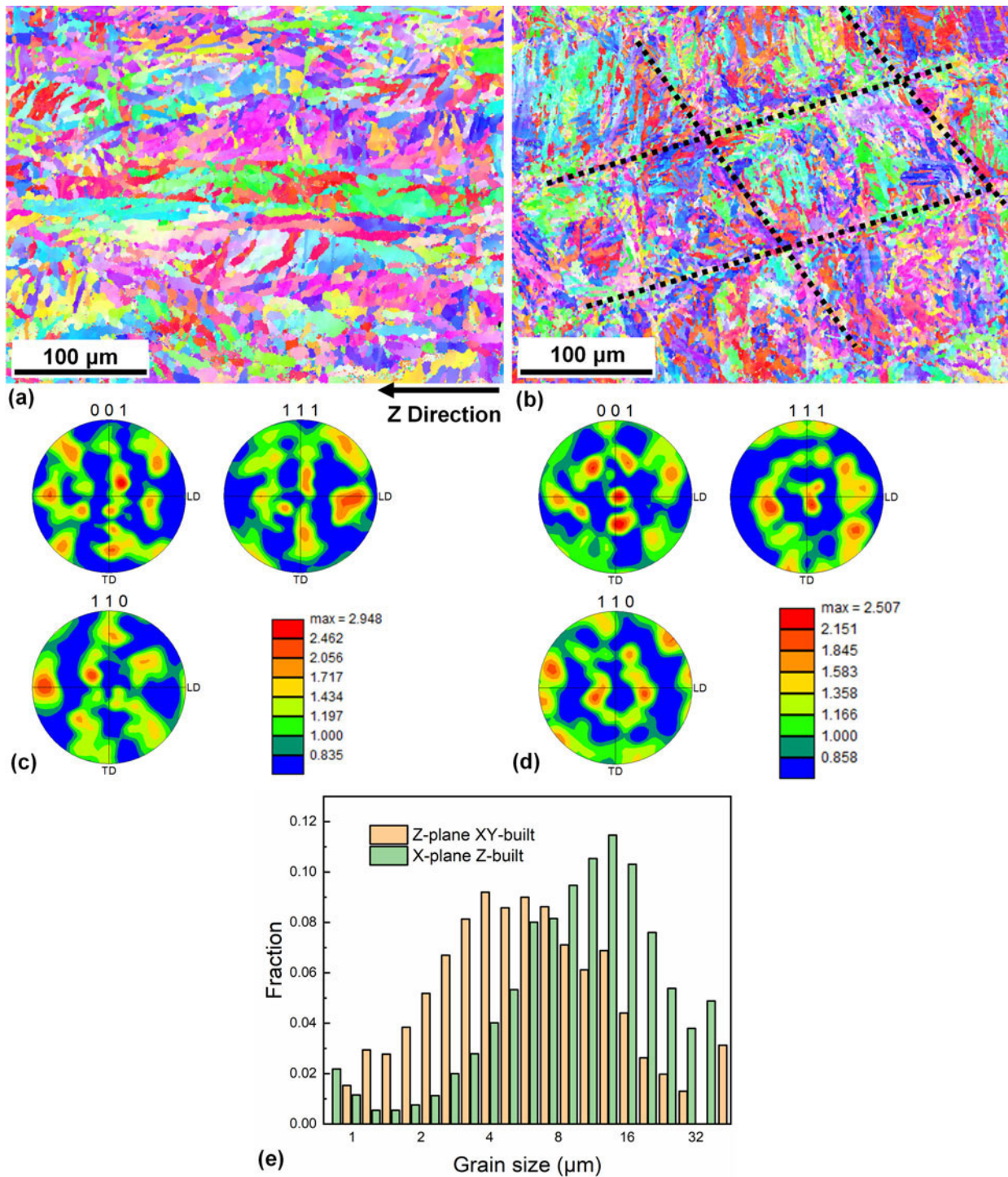


Figure 5. The EBSD analysis of the as-built 18Ni-300 maraging samples: (a,c) the X-plane of the Z-built sample and (b,d) the Z-plane of the XY-built sample, and (e) the Z-plane. (e) The distribution of grain sizes of the two samples.

the higher uniform elongation (EL) in the XY-built sample than the Z-built sample.

The fractographic images of the as-built 18Ni-300 MS sample are shown in Fig. 7. Dimple-like morphology was observed

in Figs. 7(a) and 7(b), which demonstrate that ductile failure and extensive plastic deformation occurred before fracture. This is consistent with the large elongation value. In addition, the micro-sized balling defect was also observed in the fracture

TABLE I Mechanical properties of the SLM 18Ni-300 MS samples.

Tensile properties									
References	Sample	E (GPa)	σ_y (MPa)	σ_{UTS} (MPa)	EL (%)	ϵ (%)			
This study	Z-built	172 ± 3.8	832 ± 3.9	1038 ± 2.7	2.4 ± 0.1	10.0 ± 0.1			
	XY-built	157 ± 3.2	1027 ± 11.7	1123 ± 15.1	3.4 ± 0.2	12.0 ± 0.3			
[43]	Conventional	180	798 ± 60	981 ± 49	–	10 ± 1.6			
[43]	Conventional (Heat treated)		1645 ± 56	1877 ± 51	–	6 ± 0.1			
Microhardness, HV									
Sample	XY-built		Z-built						
			Bottom	Middle		Top			
Plane	X	Z	X	Z	X	Z	X	Z	
HV-2 kgf	404 ± 3	393 ± 2	377 ± 6	382 ± 5	335 ± 8	336 ± 12	337 ± 6	328 ± 7	
Difference in X and Z	1.38%		0.39%		2.50%		4.06%		
Average	398 ± 6		349 ± 23						
[44]	382		375						
[45]	364		370						

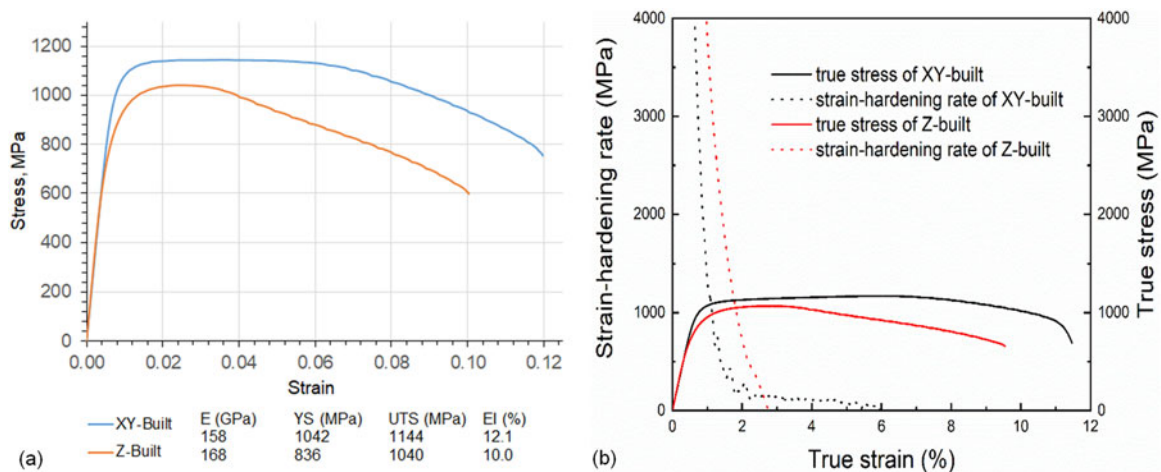


Figure 6. (a) The engineering strain–stress curves of the two samples and (b) the true strain–stress curves of the two samples and the strain hardening rate versus true strain.

surface, as marked by the yellow circle. Deep holes marked within the white circle result from the SLM process caused by molten liquid shrinkage or vaporization holes [25].

Conclusion

In this study, the 18Ni-300 MS tensile testing coupons were vertically and horizontal fabricated by laser PBF-AM process to investigate the effects of built orientation and built height on the microstructure and mechanical properties. According to the experimental results measured by OM, SEM, EBSD, tensile, and hardness tests, the major findings are summarized below:

- (i) The 18-300 MS samples with high part quality were successfully fabricated using the SLM process, and enhanced mechanical performance was obtained with yield strength ~1027 MPa, tensile strength ~1123 MPa,

hardness ~393 HV-2 kg, and strain to failure ~12.0% when compared with traditional counterparts under the same condition (i.e., yield strength ~798 MPa, tensile strength ~981 MPa, and strain to failure ~10%).

- (ii) The microstructure of the as-fabricated samples is characterized, exhibiting the primary α -martensite phase with fine cellular microstructure and the retained austenite γ phase aggregated at the boundaries of the cellular microstructure. The microstructure shows two distinct morphologies, equiaxed versus columnar substructure, resulting from the heat input distribution, temperature gradient, and growth rate. Statistical analysis shows that the spacing of fine cellular substructure in the range of 0.66–0.83 μm .
- (iii) Random grain orientations with weak textures were revealed in the as-built samples, which is attributed to the beam scanning pattern (67° rotation). In addition, the X-plane of the Z-built sample shows a relatively larger

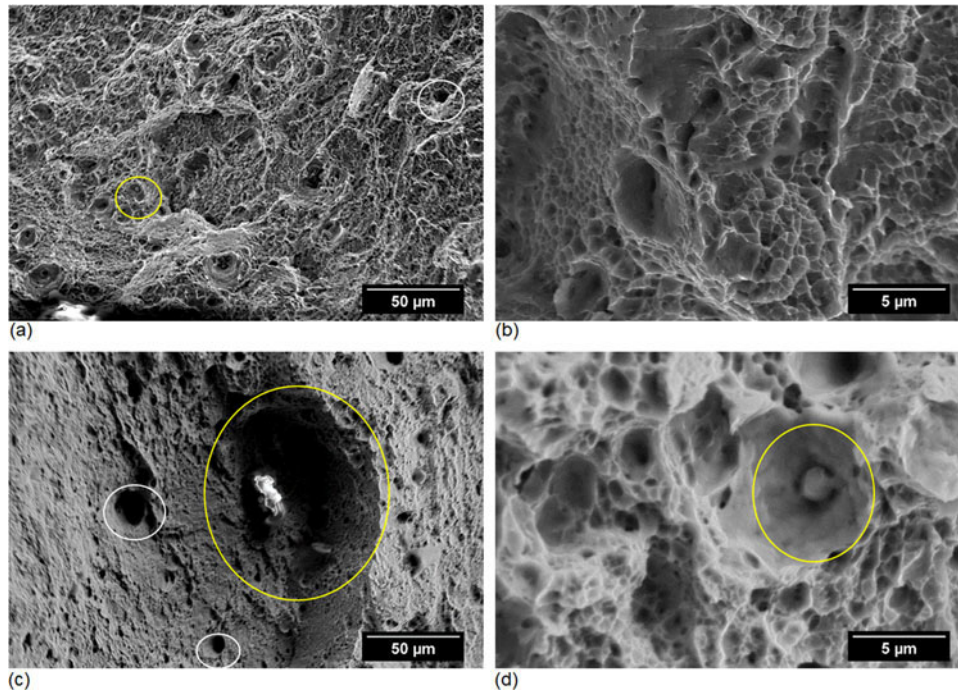


Figure 7. Fracture morphology of the XY-built sample under (a) low magnification and (b) high magnification and the Z-built sample under (c) low magnification and (d) high magnification. Note: yellow circles mean the micro-sized balling defect and white circles mean the deep holes.

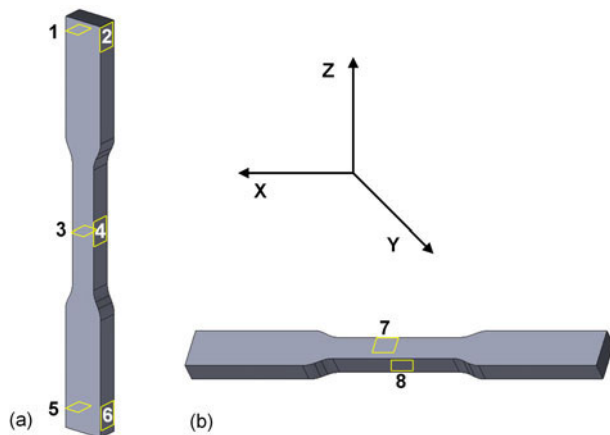


Figure 8. The 3D model of the 18Ni-300 MS block and the location of the specimens cut from the denoted blocks (a) vertical built sample (Z-built) and horizontal built sample (XY-built). Note: Z-plane (beam scanning surface) specimens: #1, #3, #5, and #7. X-plane (side surface) specimens: #2, #4, #6, and #8.

grain size ($14.36\ \mu\text{m}$) than that of the Z-plane of the XY-built sample ($6.68\ \mu\text{m}$).

- (iv) The built orientation changes the configuration of the melt pool in the as-built samples and also has a noticeable effect on the microstructure. The XY-built sample shows better tensile performance (tensile strength $\sim 1123\ \text{MPa}$ and ductility $\sim 12.0\%$) than that of the Z-built sample (tensile strength $\sim 1038\ \text{MPa}$ and ductility $\sim 10.0\%$), which could be attributed to the differences in orientations of the

cellular dendrites, the retained γ phase fractions, and the melt pool configurations induced by the built directions.

- (v) Slight anisotropy (4.06%) exists in different directions of the print samples. Along the built height direction, the bottom part has a higher value in hardness than those in the middle and top parts. This may be contributed to the finer cellular structure in the bottom part due to the high cooling rate during the solidification process.

Materials and Methods

The pre-alloyed 18Ni-300 MS powder from EOS, named as MS1, was adopted to fabricate the 18Ni-300 MS sample by an EOS M290 machine at Jacksonville State University (Jacksonville, AL). The particle size is in the range of $15\text{--}62\ \mu\text{m}$ and the chemical composition of the raw powder in weight percent is available in the material sheet [53]. As shown in Fig. 8, to study the effects of built orientation and built height on the microstructure and property anisotropy of MS alloy, two sets of tensile testing coupons with different orientations were picked. They have a gauge section of 25 mm in length, 6 mm in width, and 4 mm in thickness, respectively, which were chosen by following the requirements of the ASTM-E8M standard [54]. The coupons were built by following the process parameters in the machine defined by EOS GmbH, namely a layer thickness of $40\ \mu\text{m}$, a scan speed of $960\ \text{mm/s}$, a hatch distance of $0.11\ \text{mm}$ for the applied stripes

TABLE II Manufacturing process parameters used in fabricating 18Ni-MS300 samples.

System	Laser type	Power (W)	Layer thickness (μm)	Hatch spacing (μm)	Scanning speed (mm/s)	Scanning strategy
EOS M 290	Yb fiber	380	40	110	960	Stripes hatch strategy

hatch strategy, and 380 W of laser power, as listed in Table II. During the manufacturing process, the stripes hatch pattern was rotated 67° with respect to the former layer.

Two sets of tensile specimens were cut by a precision low-speed saw from the as-built block part to investigate the evolution of the microstructure in the *X*-plane (side surface, or *YZ*-plane) and the *Z*-plane (beam scanning surface, or *XY*-plane), as shown in Fig. 8. The sample surfaces were prepared with the standard metallographic procedures (grinding followed by fine polishing down to $0.05\ \mu\text{m}$ colloidal alumina) for microstructure analysis and the microhardness tests. Microstructural examinations were performed by OM (Nikon Model Epiphot 200, Tokyo, Japan), XRD (X'Pert MPD, Philips, Amsterdam, Netherlands), Apreo field emission SEM (Thermo Scientific™, Waltham, Massachusetts), and EBSD (Helios 600 FIB machine equipped with an EBSD detector from EDAX, Waltham, Massachusetts).

The microhardness tests of the specimens were performed using a Vickers hardness indenter (Buehler Inc., Lake Bluff, Illinois) with a load of 2000 gf and dwell time of 10 s. The reported hardness values correspond to the average value of five separate tests. The tensile tests were performed according to ASTM at a strain of 1 mm/min [55] using the MTS Landmark Servohydraulic test system and repeated three times.

Acknowledgments

The work was supported by the Faculty Research Grant Award at Jacksonville State University. L.L. acknowledges the support by the NASA EPSCoR award NNX15AK29A with the sub-award No.: 2016-045.

References

- A. Standard:** Standard Terminology for Additive Manufacturing Technologies (ASTM International F2792-12a, West Conshohocken, PA, 2012).
- X. Wang and K. Chou:** Effect of support structures on Ti-6Al-4 V overhang parts fabricated by powder bed fusion electron beam additive manufacturing. *J. Mater. Process. Technol.* **257**, 65 (2018).
- Z. Wang, K. Guan, M. Gao, X. Li, X. Chen, and X. Zeng:** The microstructure and mechanical properties of deposited-IN718 by selective laser melting. *J. Alloys Compd.* **513**, 518 (2012).
- X. Wang, T. Keya, and K. Chou:** Build height effect on the Inconel 718 parts fabricated by selective laser melting. *Procedia Manuf.* **5**, 1006 (2016).
- K.D. Ramkumar, B.M. Kumar, M.G. Krishnan, S. Dev, A.J. Bhalodi, N. Arivazhagan, and S. Narayanan:** Studies on the weldability, microstructure and mechanical properties of activated flux TIG weldments of Inconel 718. *Mater. Sci. Eng. A* **639**, 234 (2015).
- D. Ma, A.D. Stoica, Z. Wang, and A.M. Beese:** Crystallographic texture in an additively manufactured nickel-base superalloy. *Mater. Sci. Eng. A* **684**, 47 (2017).
- Z. Qian, S. Chumbley, and E. Johnson:** The effect of specimen dimension on residual stress relaxation of carburized and quenched steels. *Mater. Sci. Eng. A* **529**, 246 (2011).
- L. Santos, L. Borrego, J. Ferreira, J. de Jesus, J. Costa, and C. Capela:** Effect of heat treatment on the fatigue crack growth behaviour in additive manufactured AISI 18Ni300 steel. *Theor. Appl. Fract. Mech.* **102**, 10 (2019).
- M. Åsberg, G. Fredriksson, S. Hatami, W. Fredriksson, and P. Krakhmalev:** Influence of post treatment on microstructure, porosity and mechanical properties of additive manufactured H13 tool steel. *Mater. Sci. Eng. A* **742**, 584 (2019).
- H. Azizi, R. Ghiaasiaan, R. Prager, M. Ghoncheh, K.A. Samk, A. Lausic, W. Byleveld, and A. Phillion:** Metallurgical and mechanical assessment of hybrid additively-manufactured maraging tool steels via selective laser melting. *Addit. Manuf.* **27**, 389 (2019).
- E.A. Jägle, P.-P. Choi, J. Van Humbeeck, and D. Raabe:** Precipitation and austenite reversion behavior of a maraging steel produced by selective laser melting. *J. Mater. Res.* **29**, 2072 (2014).
- S. Bodziak, K.S. Al-Rubaie, L. Dalla Valentina, F.H. Lafratta, E.C. Santos, A.M. Zanatta, and Y. Chen:** Precipitation in 300 grade maraging steel built by selective laser melting: Aging at 510 C for 2 h. *Mater. Charact.* **151**, 73 (2019).
- C. Tan, K. Zhou, W. Ma, P. Zhang, M. Liu, and T. Kuang:** Microstructural evolution, nanoprecipitation behavior and mechanical properties of selective laser melted high-performance grade 300 maraging steel. *Mater. Des.* **134**, 23 (2017).
- C. Liu, Z. Cai, Y. Dai, N. Huang, F. Xu, and C. Lao:** Experimental comparison of the flow rate and cooling performance of internal cooling channels fabricated via selective laser melting and conventional drilling process. *Int. J. Adv. Manuf. Technol.* **96**, 2757 (2018).

15. **Y. Bai, Y. Yang, Z. Xiao, and D. Wang:** Selective laser melting of maraging steel: Mechanical properties development and its application in mold. *Rapid Prototyp. J.* **24**, 623 (2018).
16. **A. Suzuki, R. Nishida, N. Takata, M. Kobashi, and M. Kato:** Design of laser parameters for selectively laser melted maraging steel based on deposited energy density. *Addit. Manuf.* **28**, 160 (2019).
17. **Z. Qian, S. Chumbley, T. Karakulak, and E. Johnson:** The residual stress relaxation behavior of weldments during cyclic loading. *Metall. Mat. Trans. A* **44**, 3147 (2013).
18. **J. Mutua, S. Nakata, T. Onda, and Z.-C. Chen:** Optimization of selective laser melting parameters and influence of post heat treatment on microstructure and mechanical properties of maraging steel. *Mater. Des.* **139**, 486 (2018).
19. **F.F. Conde, J.D. Escobar, J. Oliveira, M. Béres, A.L. Jardini, W.W. Bose, and J.A. Avila:** Effect of thermal cycling and aging stages on the microstructure and bending strength of a selective laser melted 300-grade maraging steel. *Mater. Sci. Eng. A* **758**, 192 (2019).
20. **R. Casati, J.N. Lemke, A. Tuissi, and M. Vedani:** Aging behaviour and mechanical performance of 18-Ni 300 steel processed by selective laser melting. *Metals* **6**, 218 (2016).
21. **K. Monkova, I. Zetkova, L. Kučerová, M. Zetek, P. Monka, and M. Daña:** Study of 3D printing direction and effects of heat treatment on mechanical properties of MS1 maraging steel. *Arch. Appl. Mech.* **89**, 791 (2019).
22. **B. Mooney, K.I. Kourousis, and R. Raghavendra:** Plastic anisotropy of additively manufactured maraging steel: Influence of the build orientation and heat treatments. *Addit. Manuf.* **25**, 19 (2019).
23. **C. Tan, K. Zhou, M. Kuang, W. Ma, and T. Kuang:** Microstructural characterization and properties of selective laser melted maraging steel with different build directions. *Sci. Technol. Adv. Mater.* **19**, 746 (2018).
24. **S. Yin, C. Chen, X. Yan, X. Feng, R. Jenkins, P. O'Reilly, M. Liu, H. Li, and R. Lupoi:** The influence of aging temperature and aging time on the mechanical and tribological properties of selective laser melted maraging 18Ni-300 steel. *Addit. Manuf.* **22**, 592 (2018).
25. **Y. Bai, D. Wang, Y. Yang, and H. Wang:** Effect of heat treatment on the microstructure and mechanical properties of maraging steel by selective laser melting. *Mater. Sci. Eng. A* **760**, 105 (2019).
26. **EOS GmbH:** Material Data Sheet EOSINT M 280 EOSINT M 270 (2011). http://ip-saas-eos-cms.s3.amazonaws.com/public/1af123af9a636e61/042696652ecc69142c8518dc772dc113/EOS_MaragingSteel_MS1_en.pdf
27. **Z. Wang, T.A. Palmer, and A.M. Beese:** Effect of processing parameters on microstructure and tensile properties of austenitic stainless steel 304L made by directed energy deposition additive manufacturing. *Acta Mater.* **110**, 226 (2016).
28. **P. Wang, P. Huang, F.L. Ng, W.J. Sin, S. Lu, M.L.S. Nai, Z. Dong, and J. Wei:** Additively manufactured CoCrFeNiMn high-entropy alloy via pre-alloyed powder. *Mater. Des.* **168**, 107576 (2019).
29. **P. Wang, J. Song, M.L.S. Nai, and J. Wei:** Experimental analysis of additively manufactured component and design guidelines for lightweight structures: A case study using electron beam melting. *Addit. Manuf.* **33**, 101088 (2020).
30. **A. Kaplan:** A model of deep penetration laser welding based on calculation of the keyhole profile. *J. Phys. D: Appl. Phys.* **27**, 1805 (1994).
31. **C. Panwisawas, B. Perumal, R.M. Ward, N. Turner, R.P. Turner, J.W. Brooks, and H.C. Basoalto:** Keyhole formation and thermal fluid flow-induced porosity during laser fusion welding in titanium alloys: Experimental and modelling. *Acta Mater.* **126**, 251 (2017).
32. **P. Wang, M.H. Goh, Q. Li, M.L.S. Nai, and J.J.V. Wei:** Effect of defects and specimen size with rectangular cross-section on the tensile properties of additively manufactured components. *Virtual and Physical Prototyping* **1**, 1 (2020).
33. **P. Li, D. Warner, J. Pegues, M. Roach, N. Shamsaei, and N. Phan:** Investigation of the mechanisms by which hot isostatic pressing improves the fatigue performance of powder bed fused Ti-6Al-4 V. *Int. J. Fatigue* **120**, 342 (2019).
34. **S.L. Lu, H.P. Tang, S.M.L. Nai, Y.Y. Sun, P. Wang, J. Wei, and M. Qian:** Intensified texture in selective electron beam melted Ti-6Al-4 V thin plates by hot isostatic pressing and its fundamental influence on tensile fracture and properties. *Mater. Charact.* **152**, 162 (2019).
35. **X. Wang and K. Chou:** Effects of thermal cycles on the microstructure evolution of Inconel 718 during selective laser melting process. *Addit. Manuf.* **18**, 1 (2017).
36. **S. Holland, X. Wang, J. Chen, W. Cai, F. Yan, and L. Li:** Multiscale characterization of microstructures and mechanical properties of Inconel 718 fabricated by selective laser melting. *J. Alloys Compd.* **784**, 182 (2019).
37. **X. Wang and K. Chou:** Microstructure simulations of Inconel 718 during selective laser melting using a phase field model. *Int. J. Adv. Manuf. Technol.* **100**, 2147 (2019).
38. **E. Hall:** The deformation and ageing of mild steel: III discussion of results. *Proc. Phys. Soc. B* **64**, 747 (1951).
39. **A. Hozoorbakhsh, M.I.S. Ismail, and N.B.A. Aziz:** A computational analysis of heat transfer and fluid flow in high-speed scanning of laser micro-welding. *Int. Commun. Heat Mass Transf.* **68**, 178 (2015).
40. **H. Tan, Z. Luo, Y. Li, F. Yan, R. Duan, and Y. Huang:** Effect of strengthening particles on the dry sliding wear behavior of Al₂O₃-

- M₇C₃/Fe metal matrix composite coatings produced by laser cladding. *Wear* **324**, 36 (2015).
41. **C. Todaro, M. Easton, D. Qiu, D. Zhang, M. Bermingham, E. Lui, M. Brandt, D. StJohn, and M. Qian:** Grain structure control during metal 3D printing by high-intensity ultrasound. *Nat. Commun.* **11**, 1 (2020).
 42. **L.N. Carter, C. Martin, P.J. Withers, and M.M. Attallah:** The influence of the laser scan strategy on grain structure and cracking behaviour in SLM powder-bed fabricated nickel superalloy. *J. Alloys Compd.* **615**, 338 (2014).
 43. **L. Kučerová, I. Zetková, A. Jandová, and M. Bystrianský:** Microstructural characterisation and in-situ straining of additive-manufactured X3NiCoMoTi 18-9-5 maraging steel. *Mater. Sci. Eng. A* **750**, 70 (2019).
 44. **B. Mooney, K.I. Kourousis, R. Raghavendra, and D. Agius:** Process phenomena influencing the tensile and anisotropic characteristics of additively manufactured maraging steel. *Mater. Sci. Eng. A* **745**, 115 (2019).
 45. **G. Meneghetti, D. Rigon, D. Cozzi, W. Waldhauser, and M. Dabalà:** Influence of build orientation on static and axial fatigue properties of maraging steel specimens produced by additive manufacturing. *Procedia Struct. Integr.* **7**, 149 (2017).
 46. **T.H. Becker and D. Dimitrov:** The achievable mechanical properties of SLM produced maraging steel 300 components. *Rapid Prototyp. J.* **22**, 487 (2016).
 47. **J. Suryawanshi, K. Prashanth, and U. Ramamurty:** Tensile, fracture, and fatigue crack growth properties of a 3D printed maraging steel through selective laser melting. *J. Alloys Compd.* **725**, 355 (2017).
 48. **Renishaw:** Maraging Steel M300 Powder for Additive Manufacturing (2017); p. 1. <http://resources.renishaw.com/en/download/data-sheet-maraging-steel-m300-for-400-w-powder-for-additive-manufacturing--96326>.
 49. **Y. Bai, Y. Yang, D. Wang, and M. Zhang:** Influence mechanism of parameters process and mechanical properties evolution of maraging steel 300 by selective laser melting. *Mater. Sci. Eng. A* **703**, 116 (2017).
 50. **J. Tian, Z. Huang, W. Qi, Y. Li, J. Liu, and G. Hu:** Dependence of microstructure, relative density and hardness of 18Ni-300 maraging steel fabricated by selective laser melting on the energy density. In *Advances in Materials Processing: Proceedings of Chinese Materials Conference 2017* (Springer, Singapore, 2018); p. 229.
 51. **A.G. Demir and B. Previtali:** Investigation of remelting and pre-heating in SLM of 18Ni300 maraging steel as corrective and preventive measures for porosity reduction. *Int. J. Adv. Manuf. Technol.* **93**, 2697 (2017).
 52. **L. Roy:** *Variation in Mechanical Behavior due to Different Build Directions of Ti6Al4 V Fabricated by Electron Beam Additive Manufacturing Technology* (University of Alabama Libraries, Tuscaloosa, AL, 2013).
 53. **EOS GmbH:** Material Data Sheet EOS M 290 – EOS Maraging Steel MS1 (2017); p. 1. https://cdn.eos.info/1deee2b550955632/b3615b80c80a/MS-MS1-M290_Material_data_sheet_10-17_en.pdf.
 54. **E. ASTM:** Standard Test Methods for Tension Testing of Metallic Materials. Annual Book of ASTM Standards. (ASTM, West Conshohocken, PA, 2001).
 55. **A. Standard:** E8. Standard Test Method for Tension Testing of Metallic Materials (ASTM, West Conshohocken, USA, 2004).